ACS APPLIED MATERIALS & INTERFACES

Research Article

www.acsami.org

Carbon Nitride Nanosheet-Supported Porphyrin: A New Biomimetic Catalyst for Highly Efficient Bioanalysis

Shengyuan Deng,[†,‡,§] Peixin Yuan,[†,§] Xubo Ji,[†] Dan Shan,*[,†] and Xueji Zhang[†]

[†]School of Environmental and Biological Engineering, Nanjing University of Science and Technology, Nanjing 210094, P. R. China

[‡]State Key Laboratory of Analytical Chemistry for Life Science, School of Chemistry and Chemical Engineering, Nanjing University, Nanjing 210093, P. R. China

ABSTRACT: A highly efficient biomimetic catalyst was fabricated based on ultrathin carbon nitride nanosheets (C_3N_4)-supported cobalt(II) *proto*-porphyrin IX (CoPPIX). The periodical pyridinic nitrogen units in C_3N_4 backbone could serve as electron donors for great affinity with Co^{2+} in PPIX, which resembled the local electronic structure as vitamin B12 and heme cofactor of hemoglobin. UV−vis kinetics and electrochemistry revealed its competitive (electro)-catalysis with conventional peroxidase, while X-ray photoelectron spectroscopy and theoretical calculations suggest that the rehybridization of Co 3d with N orbitals from the backside can result in significant changes in enthalpy and charge density, which greatly promoted the activity of CoPPIX. The prepared nanocatalyst was further conjugated with streptavidin via multiple amines on the edge plane of C_3N_4 for facile tagging. Using biotinylated molecular beacon as the capture probe, a sensitive electrochemiluminescence-based DNA assay was developed via the electroreduction of H_2O_2 as the coreactant after the hairpin unfolded by the target, exhibiting linearity from 1.0 fM to 0.1 nM and a detection limit of 0.37 fM. Our results demonstrate a new paradigm to rationally design inexpensive and durable biomimics for electrochemiluminescence quenching strategy, showing great promise in bioanalytical applications.

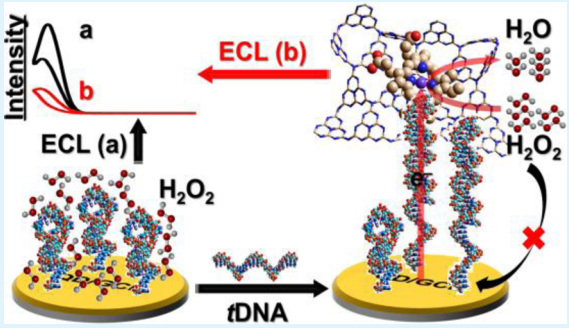

KEYWORDS: *biomimetic catalyst, carbon nitride, cobalt porphyrin, hydrogen peroxide, electrochemiluminescence, electrocatalysis*

1. INTRODUCTION

Highly sensitive and selective determination of nucleotides is essential to many areas, such as disease diagnosis, biomedical research, and biodefense applications.[1−3] Great efforts, including fluorescent, electrochemical, chemiluminescent, and photoelectrochemical techniques, have endeavored to develop ultrasensitive DNA sensors especially for the detection of low-abundance nucleotides in human serum and cytoplasm.[4−6] Owing to its electrodriven nature, electrochemiluminescence (ECL) features intrinsically low background thus has realized ultrasensitive DNA assays.[7] One major protocol utilizes bioengineered enzyme-linked probes, converting the amount of substrates, for example, O_2 and H_2O_2, as coreactants in the cathodic pathway, into target-concentration-dependent "signal-off".[8] However, the catalytic activity of natural enzymes is susceptible to environment. Besides, although the combination of multienzyme labeling and molecular mediators like hydroquinone could amplify the detection signal,[9,10] the large occupied volume of proteins restrains loading capacity,[11−13] while the problems of operational stability and cost arose in the meantime. Hence, searching for alternatives is of great importance to enhance the performance in bioassays.

Since conventional enzymes such as hemoglobin, cytochrome *c* oxidase, horseradish peroxidase (HRP), etc. encapsulate porphyrin cofactors, structural and functional biomimicry by extraction and recombination of porphyrin complexes has drawn much attention.[14−16] For example, hemin-*G*-quadruplex has been considered as a successful artificial DNAzyme by separate accommodation of porphyrin molecule.[17,18] However, its catalytic activity could hardly match up with that of natural enzymes, because the embedded porphyrins within are five-coordinated with an axial ligand of proximal histidine from backside peptide.[19,20] Enzymatic studies have proved that this axial coordination serves multiple functions to enhance the catalytic characteristics.[21,22] Thus, restoring the primitive chemical configuration was intended during the rational design of biomimics in terms of preserving intrinsic activity.[23]

Given the very essence of axial ligation is one back-up electron pair, two-dimensional carrier as open accessible π-donors could mimic the role of cysteine or histidine in proteins for the assembly of metalloporphyrin through cation-π interactions,[24,25] such as graphene-supported hemin, whose catalytic activity was improved remarkably toward the oxidization of pyrogallol.[26,27] Inspiringly, the N-doped carbon nitride nanosheets (C_3N_4) derived from a one-step synthesis could be a potential candidate with periodical pyridinic nitrogen. The abundant unsaturated Ns of more electro-

Received: September 30, 2014
Accepted: December 12, 2014
Published: December 12, 2014

 © 2014 American Chemical Society

negativity than C also make C_3N_4 a Lewis base nucleophilic to metal ions.[28,29] This motivated us to fabricate a novel and low-cost peroxidase-like catalyst by integrating C_3N_4, hollow *proto*-porphyrin IX (PPIX), and cobalt(II) cation (Co^{II}) into a CoPPIX@C_3N_4 composite (Scheme 1), as corrin ring is the center of vitamin B12, which involves in methylmalonyl CoA mutase and methyltransferase family reactions in humans,[30,31] and Co^{II} inherently owns an active reactivity.

Scheme 1. Schematic Illustration of the Preparation of CoPPIX@C_3N_4 for Ultrasensitive DNA Detection via the Consumption of Coreactant

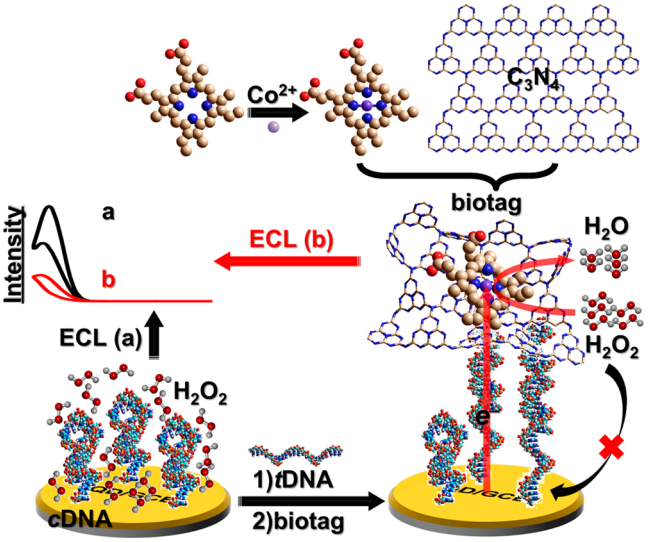

A rehybridization of Co 3d with N 1s orbitals and a significant change in localized charge density were inferred from the simulative modeling of CoPPIX@C_3N_4 composite. This validated its superior catalytic properties comparable to HRP. The thermal oxidation of C_3N_4 also produced adequate amines on the edge plane, facilitating the subsequent labeling of CoPPIX@C_3N_4 with streptavidin. An ultrasensitive analytical strategy was thus proposed for the detection of DNA via electrocatalytic reduction of H_2O_2 by CoPPIX@C_3N_4 probe (Scheme 1). Using molecular beacon as the capture probe (*c*DNA), the recognition of complementary target DNA (*t*DNA) unfolded the hairpin, exposing the biotinylated 5′ extremity. CoPPIX@C_3N_4 was then concentrated in the sensing interface via biotin−streptavidin interaction. Multiple CoPPIX electrochemically consumed H_2O_2 as the ECL coreactant, leading to drastic annihilation in emission. This strategy could detect DNA sequence down to femtomolar level with a linear range over 6 orders of magnitude. The proposed system provided a paradigm for rational design of natural enzyme substitutes and could be easily expanded to signal amplification of ECL bioassay and other biomedical applications.

2. EXPERIMENTAL SECTION

2.1. Chemical Reagents. Tween-20, chitosan (≥85%, deacetylation), bovine serum albumin (BSA), 2,3-dimercapto-1-propanesulfonate sodium monohydrate (DMPS), *N*-2-(4-morpholino)-ethanesulfonic acid (MES), tri(2-carboxyethyl)phosphine hydrochloride (TCEP), 1-ethyl-3-(3-(dimethylamino)propyl)carbodiimide (EDC), *N*-hydroxysulfosuccinimide (NHS), *p*-phenylene di-*iso*-thiocyanate (PDITC, 98%), pyrogallol, HRP (E.C. 1.11.1.7), melamine (≥99.9%), and tris(hydroxymethyl)aminomethane (Tris) were procured from Sigma-Aldrich Chemical Co., Ltd. (Shanghai, China). $CdCl_2{\cdot}2.5H_2O$, $CoCl_2$ and glutaraldehyde (25% aqueous solution) were purchased from Alfa Aesar Co., Ltd. (Tianjin, China). PPIX (98%) was ordered from J&K Scientific Ltd. (Shanghai, China). The synthetic single-stranded oligonucleotides were purchased from Sangon Biological Engineering Technology & Services Co. Ltd. (Shanghai, China). To reduce disulfide bonds, 37.8 μL of 1 μM *c*DNA was activated with 1.5 μL of 10 mM TCEP prior to usage.Their sequences are listed in Table 1. Streptavidin and HRP-labeled streptavidin (strept-HRP) were bought from Promega Biological Product Co., Ltd. (Shanghai, China) and CanAg Diagnostics Inc. (Göthenburg, Sweden), respectively. All other reagents were of analytical grade and used as received.

Table 1. Oligonucleotide Sequences

*c*DNA	5′−biotin−**GCA TAT TTT GTC CAT ATG AGA TCT AAA ATA TGC** AAA AA−$(CH_2)_6$−NH_2−3′
*t*DNA	5′−**AGA TCT CAT ATG GAC AAA ATA TGC**−3′
1-base mismatch	5′−AGA T**A**T CAT ATG GAC AAA ATA TGC−3′
2-base mismatch	5′−AGA T**A**T CAT **G**TG GAC AAA ATA TGC−3′
3-base mismatch	5′−AGA T**A**T CAT **G**TG GAC AA**C** ATA TGC−3′

Ultrapure water obtained from a Millipore water purification system (≥18 MΩ, Milli-Q) was implemented throughout all assays. 0.1 M phosphate buffer saline (PBS) solutions with various pH values were prepared by mixing the stock solutions of 0.1 M NaH_2PO_4 and 0.1 M Na_2HPO_4 with 0.1 M KNO_3 as the supporting electrolyte and employed as detection solutions. For consistency with literature values,[19,32] 10 mM pH 7.4 PBS was applied as diluent in UV−vis kinetic tests and as washing buffer in DNA hybridization. 0.05% (w/v) Tween-20 in 10 mM pH 7.4 PBS (PBST) was taken for protein dissolution and biotin−streptavidin interaction. The blocking solution was 10 mM pH 7.4 PBS containing 2% (w/v) BSA. The O_2 or N_2-saturated solution was prepared by bubbling highly pure O_2 or N_2 into the solution for 30 min and preserving its atmospheric pressure.

2.2. Apparatus. UV−vis absorption spectra were recorded on a UV-3600 UV−vis−near-IR spectrophotometer (Shimadzu Co., Japan). Attenuated total reflection Fourier-transformation infrared (ATR-FTIR) spectra were obtained with an IR-Prestige-21 FTIR spectrometer (Shimadzu Co., Japan). X-ray photoelectron spectra (XPS) were examined on a K-α X-ray photoelectron spectrometer (Thermo Fisher Scientific Co., U.S.A.). The transmission electron micrographs (TEM) were taken using a TECNAI-12 TEM instrument (Philips, U.K.). Tapping mode atomic force microscopic (AFM) images were acquired by an Agilent 5500 AFM/SPM system (U.S.A.) with Picoscan v5.3.3 software.

Electrochemical experiments were performed on a CHI 660D electrochemical workstation (Shanghai Chenghua Instruments Inc., China). Surface plasmon resonance (SPR) spectra were plotted on an ESPRIT SPR.B.V spectrometer with Data Acquisition v1.9 package. ECL measurements were carried out on an MPI-E multifunctional electrochemical and chemiluminescent analytical system (Xi'an Remex Analytical Instrument Co., Ltd., China) in which the emission window lays above the photomultiplier tube biased at −800 V. Conventional three-electrode configuration consisting of a modified glassy carbon electrode (GCE, 5 mm in diameter) as working electrode, a platinum wire as counter electrode, and a Ag/AgCl electrode as reference electrode were placed in a homemade electrochemical cell. Unless specifically mentioned, the scan rate was 100 mV s^{-1}.

2.3. Computational Methods. Single-point calculation and geometry optimization were performed with Vienna ab initio simulation package (VASP).[25] The globally implemented molecular mechanical force field was BIO+(CHARMM) with each scale factor among distance-dependent dielectric, electrostatic, and van der Waals interaction fixed to one. The force field involved bond, angle, torsion,

nonbonded, electrostatic, and hydrogen-bonded components with none distant cut-offs. Projected augmented wave potentials were used to describe the core electrons, the Khon−Sham one-electron wave functions were expanded in a plane wave basis set with cutoff energy of 400 eV, and Polak−Ribiere conjugate gradient approximation was employed to describe the electrons exchange-correlation potential. The length of C_3N_4 in the modeling cell was sufficient to render interaction energy between adsorbate and substrate. Localized spin-polarized density functional theory (DFT)-based calculations were carried out using Gaussian 09 software.[33] B3LYP method was used with a LanL2DZ basis for Co and 6-31G* basis for the rest of atoms. The images of simulative structures were generated from HyperChem 8.5.

2.4. Preparation of C_3N_4. The generation of C_3N_4 was initiated with serial pyrolysis-thermal oxidation described below. Bulk graphitic-phase C_3N_4 was prepared by direct pyrolysis of melamine in the semiclosed system.[34] Briefly, 5.0 g of melamine was placed in a ceramic crucible covered with an aluminum-foil paper to prevent the vaporization of intermediates (e.g., (*iso*-)cyanic acids), ramped up in static air at 3 °C min^{-1}, and kept at 600 °C for 2 h; afterward, this was cooled to room temperature overnight. The resultant yellow agglomerates were milled into powder in an onyx mortar. The above product subsequently underwent a thermal oxidation, etching into ultrathin C_3N_4 nanosheets as follows:[35] ∼200 mg of bulk C_3N_4 was put in an open ceramic container and heated in static air at 500 °C for 4 h with a ramp rate of 5 °C min^{-1}. A light yellow inflated powder was achieved for immediate liquid exfoliation into C_3N_4. 1.0 mg of oxidized C_3N_4 was readily soluble in 1.0 mL of deionized water during mild ultrasonication to form a homogeneous milky dispersion. Unexfoliated C_3N_4 was removed after centrifugation at 5000 rpm for 5 min.

2.5. Preparation of CoPPIX@C_3N_4. CoPPIX was synthesized by a simple complexation reaction.[32] Briefly, 0.5 mmol of PPIX was dissolved in 10 mL of dimethylformamide (DMF), and then 0.5 mmol $CoCl_2$ was added. The mixture was stirred for 10 h at room temperature. Thereafter, the excessive solvent was gasified under vacuum desiccation at 60 °C. Finally, the crystalline CoPPIX was dissolved in DMF. CoPPIX@C_3N_4 was prepared by in situ adsorption of CoPPIX on C_3N_4 (Scheme 1). Briefly, 1.0 mL of 10 mM CoPPIX DMF solution was introduced into 1.0 mL of 1.0 mg mL^{-1} C_3N_4 in DMF. The mixture was stirred mildly for 10 h. After centrifugation to remove excessive free porphyrins and vacuum drying, CoPPIX@C_3N_4 solids were achieved.

2.6. Preparation of Streptavidin-Labeled CoPPIX@C_3N_4 Probe. 50.0 mg CoPPIX@C_3N_4 was dissolved in 1.0 mL of DMF containing 1.0 mM PDITC as coupling agent, and the mixture was under vigorous vortex for 2 h at room temperature. The suspension was centrifuged at 10000 rpm for 30 min, and then the supernatant was decanted. The remaining deposition was thoroughly washed and centrifuged three times and redispersed in ultrapure water. Next, 250 μL of 0.1 mg mL^{-1} streptavidin in 10 mM pH 7.4 PBS was mixed with the above precipitate and vortexed for 4 h at room temperature to produce streptavidin-functionalized CoPPIX@C_3N_4 (CoPPIX@C_3N_4-strept) probe. The resultant was centrifuged at 6000 rpm for 30 min, purified, and stored in solid at 4 °C prior to use. As control, C_3N_4-strept was prepared following the same course.

2.7. Fabrication of ECL DNA Sensor and Measurement Procedure. The synthesis of DMPS-stabilized CdTe QDs was developed by us and has been reported elsewhere.[36] Prior to modification, a GCE was successively polished to a mirror finish using 1.0 and 0.05 μm alumina slurry, followed by sonication in anhydrous ethanol and double-distilled water. The stepwise sensing protocol was briefed as follows:

(1) After the bare electrode was rinsed with doubly distilled water and allowed to dry in a N_2 atmosphere, 20 μL of QDs solution was dropped onto the surface and dried at room temperature. (2) 10 μL of 0.025 wt % chitosan was coated on QDs film and activated with 15 μL of 2% glutaraldehyde for 2 h. (3) The modified GCE was then incubated in 20 μL of 1.0 μM *c*DNA for 60 min at 37 °C in a 100% moisture-saturated environment. (4) Afterward, the resulting surface was slowly washed with streams of washing buffer to remove unbound oligonucleotides, blocked the nonspecific binding sites with BSA for 45 min at 37 °C, and finally rinsed with PBST and PBS. (5) For the hybridization, a 20 μL droplet of *t*DNA with different concentration from 0.1 fM to 0.1 nM was pipetted separately at each sensing interface. (6) After incubation, the biosensor was rinsed followed by incubating with 20 μL of probe at 37 °C for 30 min.

Lastly, the biosensor was eluted with PBS and subjected to ECL measurements from 0 to −1.3 V in the detection solution containing 0.5 mM H_2O_2 as the exogenous coreactant, which was deaerated with highly pure N_2 for 15 min beforehand and maintained in that atmosphere. In pratice, the exact time that it took for this new bioanalysis to complete the whole detection process was summed to be 2 h 45 min.

3. RESULTS AND DISCUSSION

3.1. Characterization of C_3N_4 and CoPPIX@C_3N_4. The morphology and microstructure of C_3N_4 were investigated with TEM and AFM as shown in Figure 1. The TEM image revealed

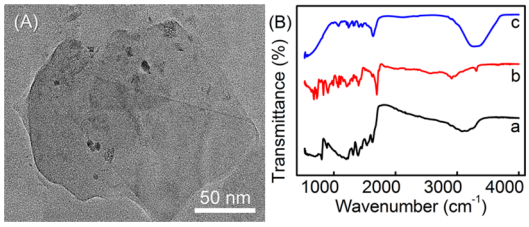

Figure 1. (A) TEM image of C_3N_4. (B) ATR-FTIR spectra of C_3N_4 (a), CoPPIX (b), and CoPPIX@C_3N_4 probe (c).

that the representative C_3N_4 appears as a planar thin nanosheet with a lateral dimension of ∼200 nm (Figure 1A), which would benefit the large accommodation of CoPPIX for the enhancement in catalytic efficiency. The assembly of porphyrin on C_3N_4 was monitored by in situ AFM-FTIR operations (Figure 1B).[26] Specifically, after C_3N_4 was deposited onto a mica sheet from aqueous solution, the tapping-mode tip scanned the well-distributed flakes and measured the thickness of ∼0.9 nm as shown in Figure 2A,C, indicating the aqueous exfoliation could easily shear C_3N_4 into small flakes with atomic monolayer nature.[34] The substrate was then immersed into CoPPIX methanol solution for in situ adsorption of CoPPIX on C_3N_4. Afterward, the appearance of exactly the same selected area became slightly rough with the thickness increased by an average of ∼0.6 nm in the corresponding horizontal and vertical cross-section profile (Figure 2B,D). As negligible change could be observed after wetting bare mica sheets with CoPPIX or after immersing C_3N_4 mica into absolute methanol and letting it vaporize as the blank (data not shown), this height increment was indeed attributed to the coating of a porphyrin monolayer on C_3N_4, which affected the force radius of AFM tip. Therefore, C_3N_4 as a support could undo the oxidative destruction of CoPPIX by blocking one side from oxidants.[26]

The chemical property of CoPPIX@C_3N_4 probe was characterized by ATR-FTIR spectroscopy (Figure 1B). The transmittance spectrum of CoPPIX (Figure 1B, curve a) illustrated the presence of C═O in carboxylic acid at 1695 cm^{-1} with fine structures of side-chain groups like carboxyethyl, vinyl, and methyl in the fingerprint region.[37] The IR spectrum of CoPPIX@C_3N_4 (Figure 1B, curve b) features a sharp peak at ∼802 cm^{-1} originated from heptazine ring (1,3,4,6,7,9,9b-heptaazaphenalene).[34] The peaks in the region from 850 to 1700 cm^{-1} are attributed to either triangular C−N(−C)−C or

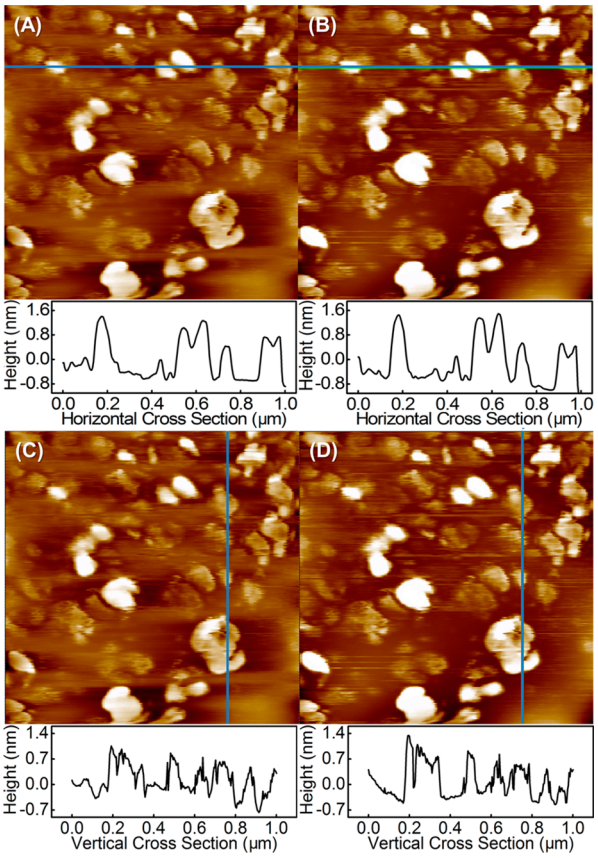

Figure 2. AFM (A, B) horizontal and (C, D) vertical topographs of C_3N_4 (A, C) before and (B, D) after the in situ adsorption of CoPPIX on mica slide, indicating monolayer assembly of molecules. Below: corresponding height profiles with *x*-axis and its increment unit represent the scan area (1.0 μm^2) and the scale bar (0.2 μm), repectively.

bridging C−NH−C units survived after thermal oxidation etching in the layers of nanosheets.[35] The broad peaks between 3000 and 3400 cm^{-1} are contributed by N−H stretching. In comparison, the FTIR spectrum of CoPPIX@C_3N_4-strept tracing tag displayed characteristic amide vibrations of proteins, for example, amide I (1633 cm^{-1}) for C═O stretching and amide II (1532 cm^{-1}) for N−H bending/C−N stretching, respectively (Figure 1B, curve c), and a broad coupling of O−H at 3309 cm^{-1}, verifying the successful linkage of streptavidin with C_3N_4.

3.2. Interaction of CoPPIX with C_3N_4. The XPS was applied to probe the interaction between CoPPIX and C_3N_4. The N 1s XPS of C_3N_4 exhibited four well-separated peaks assigned to the pyridinic, amino, pyrrolic (pyridonic), and graphitic nitrogen at 398.4, 399.1, 400.3, and 401.0 eV,[38] respectively (Figure 3A), with a relative abundance percentage of C/N to be 46.81%/50.00%, which roughly equals the ideal stoichiometric ratio of C(3)N(4). The existence of N-oxide at 404.1 eV with an additional 3.19% of O was witnessed as a result of thermal oxidation. Compared with the XPS of C_3N_4, the four fitted peaks of CoPPIX@C_3N_4 shifted to lower binding energies of 397.8, 398.6, 399.9, and 400.6 eV, respectively (Figure 3B), suggesting cation-π interaction between Co^{II} and C_3N_4 as the electron donor. The overall counts also reduced by half because of the adsorptive amount of PPIX ($C_{34}H_{34}N_4O_4$). Interestingly, the normalized atomic concentration of C 1s/N 1s/O 1s/Co 2p calculated from the XPS survey scan was

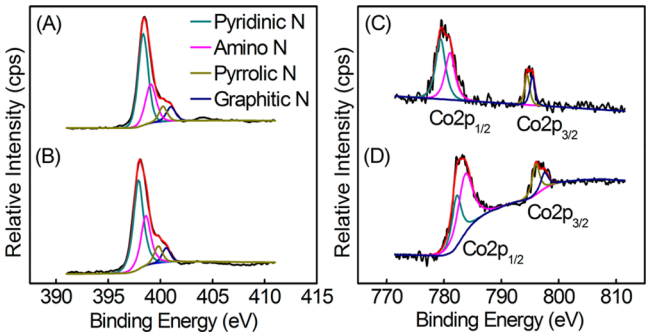

Figure 3. XPS N 1s spectra of (A) C_3N_4 and (B) CoPPIX@C_3N_4, and XPS Co 2p spectra of (C) C_3N_4 and (D) CoPPIX@C_3N_4.

52.76:29.49:16.73:1.02, coincident with the couple of every three heptazine units and one CoPPIX, suggesting an orderly assembly may be favored at the periodical structural cavity in C_3N_4. Moreover, the relative integral peak area of pyridinic/amino N dropped in comparison with that in Figure 3A, probably a consequence from the conversion of some pyridinic nitrogens into Co^{II}−N after the formation of CoPPIX@C_3N_4.[39] This interaction could be verified by contrasting Co $2p_{3/2}$ and Co $2p_{1/2}$ peaks of CoPPIX with those of CoPPIX@C_3N_4. The former dual doublets occurred at 779.4/781.0 and 794.5/795.4 eV, respectively (Figure 3C), and the latter moved to higher binding energies at 782.3/783.9 and 796.0/797.6 eV (Figure 3D), which could be ascribed to the site affinity of positively charged Co^{II} to N with high local electronegativity.[40] Thus, the proposed synthetic approach could strengthen the association of CoPPIX at C_3N_4 backbone with the help of proximal N.

The interaction between 1.0 mM CoPPIX and 0.1 mg mL^{-1} C_3N_4 was further verified by UV−vis spectra (Figure 4A). C_3N_4

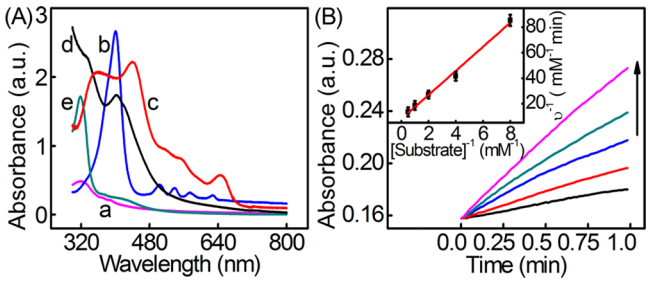

Figure 4. (A) UV−vis absorption of C_3N_4 (a), CoPPIX (b), CoPPIX@C_3N_4 (c); and the mixture of pyrogallol and H_2O_2 with CoPPIX@C_3N_4 (d) and PPIX@C_3N_4 (e). (B) The initial pyrogallol oxidation profile catalyzed by CoPPIX@C_3N_4 conjugates (5 μM CoPPIX equivalent). The concentrations of pyrogallol range from 0.1 to 2.0 mM. (inset) Lineweaver−Burk plot of the pyrogallol oxidation catalyzed by the CoPPIX@C_3N_4.

displayed a conspicuous peak at 319 nm (Figure 4A, curve a), probably due to the ordered packing of hydrogen-bond-cohered long strands of polymeric melon units.[35] CoPPIX featured an intense Soret band at 401 nm together with a series of weak Q bands at longer wavelengths of 503 and 539 nm (Figure 4A, curve b). As for the CoPPIX@C_3N_4 nanocomposite, the Soret band of CoPPIX with equivalent amount to 1.0 mM free CoPPIX was split into two adsorption peaks at λ = 358 and 441 nm in the presence of C_3N_4 (Figure 4A, curve c). The former hyperchromic effect could be attributed to the assembly of CoPPIX on C_3N_4.[41] The latter showed a decrease

in intensity with a significant red shift, thus indicating the formation of *J*-type nanoaggregates nucleated on C_3N_4 through partial π-stacking between pyrrole subunits of PPIX and heptazine of C_3N_4.[42] Compared with Figure 4A, curve a, an apparent shoulder peak was witnessed, which was dedicated to the axial ligation of Co^{II} with pyridinic nitrogen in C_3N_4. The overall absorptive bathochromicity implicated strong association between C_3N_4 and CoPPIX, which was desirable to prevent the desorption and self-dimerization of CoPPIX, hence maintaining its catalytic activity.[24] According to Beer−Lambert law, the loading capacity of CoPPIX on C_3N_4 surface was estimated to be 25.4 μmol g^{-1}.

3.3. Catalytic Activity Test. The peroxidase-like catalytic activity of CoPPIX@C_3N_4 was evaluated using an oxidation reaction of pyrogallol, which is oxidized to purpurogallin by H_2O_2.[43] The catalysis was taken place with a 5 μM equivalent of CoPPIX at 0.1, 0.2, 0.5, 1.0, and 2.0 mM pyrogallol and 40 mM H_2O_2. Since a remarkable response at 405 nm emerged in CoPPIX@C_3N_4 (Figure 4A, curve d) after the introduction of pyrogallol and H_2O_2, while PPIX@C_3N_4 did not (Figure 4A, curve e), the entire progress was tracked using UV−vis kinetic module at this wavelength to measure the instantaneous reaction rate (υ). The reacting process followed a conventional enzymatic dynamic regulation of the Michaelis−Menten equation. The Michaelis constant (K_M) and the turnover number (T_N) or catalytic constant (k_{cat}) were assessed by Lineweaver−Burk plot (eq 1) as shown in Figure 4B:

$$1/\upsilon = (K_M/V_{max})\cdot 1/[S] + 1/V_{max} \quad (1)$$

$$V_{max} = k_{cat}\cdot[E_T] \quad (2)$$

where $[S]$ and $[E_T]$ were designated as the concentration of substrate and enzyme, respectively. From the fitted line in Figure 4B inset, K_M and k_{cat} of CoPPIX@C_3N_4 were estimated to be 0.61 mM and 140.5 min^{-1}, respectively, while free CoPPIX did not show measurable catalytic parameters. The adjacent K_M values between CoPPIX@C_3N_4 and HRP demonstrated their similar affinity with H_2O_2, highlighting the importance for cofactor to retain a five-coordinated state.[19,27] The k_{cat} value nearly tripled those of MnTMPyP-*ds*DNA and hemin-*G*-quadruplex, representing higher catalytic activity.[26,37] Although k_{cat} of the proposed CoPPIX@C_3N_4 fell behind those of HRP and its mimics including hemin-graphene and FeTMPyP-antibody,[26,43] it showed better catalytic efficiency with higher apparent second-order rate constant (k_{cat}/K_M) over most tabulated data even competitive with FeTMPyP-graphene (Table 2).[44−46] In a word, considering inexpensive source and facile preparation, CoPPIX@C_3N_4 could function well as artificial enzyme with very close activity.

3.4. Electrocatalytic Kinetics of CoPPIX@C_3N_4. Since H_2O_2 is a coreactant in the cathodic route of ECL, cyclic voltammograms (CVs) of CoPPIX and CoPPIX@C_3N_4 were examined to further clarify the catalytic mechanism of H_2O_2 reduction (Figure 5A). At CoPPIX modified GCE, one pair of inflection points could be recognized at −0.273 and −0.125 V (ΔE_p = 148 mV) in N_2-saturated atmosphere (Figure 5A, curve a), which was ascribed to the electro-reduction (E_{pc}) and -oxidation (E_{pa}) of CoPPIX, respectively. By comparison, CoPPIX@C_3N_4 immobilized electrode carrying equivalent porphyrins exhibited more well-defined redox behaviors at −0.215 and −0.183 V with a relatively small potential difference (ΔE_p = 32 mV) (Figure 5A, curve b), indicating a faster electron-transfer between CoPPIX and the electrode. Moreover, the overpotential of E_{pc} was positively shifted by 58 mV, suggesting localized electronic density was thickened. This direct electrochemistry followed a surface-controlled process as both cathodic (i_{pc}) and anodic (i_{pa}) peak currents proportional to the scan rate (ν), for example, $i_{pc} = -3.559 \times 10^{-9}\nu - 3.073 \times 10^{-8}$ (R^2 = 0.998) and $i_{pa} = 3.763 \times 10^{-9}\nu - 3.356 \times 10^{-10}$ (R^2 = 0.997) (data not shown). From the equation $\alpha = |i_{pc}|/(|i_{pc}| + |i_{pa}|)$, the charge-transfer coefficient (α) turned out to be 0.51 and 0.73 with and without C_3N_4, respectively, implying better reversibility in the presence of C_3N_4. According to the Nernstian equation, ΔE_p came closer to 59/*z* mV (293 K); the charge-transfer number (*z*) should accordingly be 1, that is:

$$Co^{III} - PPIX + e^- \leftrightarrow Co^{II} - PPIX \quad (3)$$

Then the electrochemical apparent coverage (Γ_{app}) was speculated by Brown−Anson model with the formula: $i_p = (z^2F^2/4RT)\cdot\nu A\Gamma_{app}$, where *A* is the working area (diameter: 0.5 cm), ν is the scan rate (10 mV s^{-1}); *F*, *R*, and *T* represent the Faraday constant (~96 485 C mol^{-1}), the gas constant (8.314 J M^{-1} K^{-1}), and the absolute temperature (293 K), respectively. The average active surface concentration was assessed to be 9.12×10^{-3} mol cm^{-2} for CoPPIX@C_3N_4 and 5.46×10^{-3} mol cm^{-2} for CoPPIX itself. Hence, C_3N_4 as a capacious nanocarrier could not only effectively inhibit the inactive dimerization of

Table 2. Kinetic Parameters for Pyrogallol Oxidation Catalyzed by Various Catalysts

catalyst	k_{cat} [min^{-1}]	K_M [mM]	k_{cat}/K_M [$M^{-1}\cdot min^{-1}$]	ref
hemin-*G*-quadruplex	26.1	0.25	1.0×10^5	34
hemin-graphene	246	1.22	2.0×10^5	26
hemin-hydrogel	19			48
hemin	2.4			49
FeTMPyP-graphene	545	0.96	5.7×10^5	47
FeTMPyP-antibody	680	8.6	7.9×10^4	46
FeTMPyP	83			46
MnTMPyP-*ds*DNA	56.8	0.41	1.4×10^5	34
horseradish peroxidase	1750	0.81	2.2×10^6	46
CoPPIX	7.8			this work
CoPPIX@C_3N_4	140.5	0.61	2.3×10^5	this work

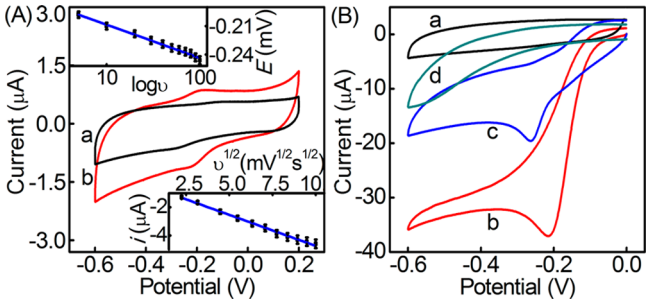

Figure 5. (A) CVs of CoPPIX (a) and CoPPIX@C_3N_4 (b) modified GCE in N_2-saturated 0.1 M pH 9.0 PBS. (B) CVs of C_3N_4 (a), CoPPIX@C_3N_4 (b), CoPPIX (c) and HRP (d) labeled streptavidin as a signal tag for the proposed DNA assay in 0.1 M pH 9.0 PBS containing 50 μM H_2O_2. The upper and lower insets are the linear fits of E_{pc} vs log(υ) and i_{pc} vs $\upsilon^{1/2}$, respectively, corresponding to curve (b) of (B).

CoPPIX, but also thicken the density of valency electrons, leading to an improved heterogeneous electron transfer.

For practical use, CoPPIX@C_3N_4 was endowed with specificity by labeling with streptavidin, which could interact with biotinylated terminal of *c*DNA (Scheme 1). Compared with the reductive incapability of H_2O_2 at C_3N_4-labeled probe in the oxygen-free environment (Figure 5B, curve a), i_{pc} of the CoPPIX@C_3N_4 tag (Figure 5B, curve b) dived as refer to Figure 5A, curve b. This diffusion-controlled process has been validated in Figure 5A, lower inset for the linearity was $i_{pc} = -4.40 \times 10^{-6} \cdot \nu^{-1/2} - 3.37 \times 10^{-6}$ ($R^2 = 0.995$). By alternating the buffer pH from 6.0 to 9.0, the corresponding E_{pc} moved positively with a fitted function: $E_{pc} = -0.0726 + 0.050 \cdot \mathrm{pH}$ ($R^2 = 0.991$) (data not shown). The number of protons participated in the elementary reaction was extracted from the slope of $E^{\Theta\prime} = K + (mRT/nF) \cdot \ln[H^+] = K - 0.058m \cdot \mathrm{pH}$ (293 K, $n = 1$), which meant H_2O_2 was reduced into H_2O as the oxidation of CoPPIX in the basic medium. Therefore, combined with eq 3, the electrochemical course could be depicted in the following equations:

$$Co^{III} - PPIX@C_3N_4 + e^- \rightarrow Co^{II} - PPIX@C_3N_4 \quad (4)$$

$$Co^{II} - PPIX@C_3N_4 + (1/2)H_2O_2 \rightarrow Co^{III} - PPIX@C_3N_4 + OH^- \quad (5)$$

The same parallel catalytic wave out of CoPPIX-strept label (Figure 5B, curve c) was barely half that at CoPPIX@C_3N_4-strept. The former E_{pc} of −0.263 V was also more negative than the latter (−0.215 V). Both inferred more efficient catalytic activity and higher loading capacity of CoPPIX on C_3N_4. Furthermore, since the coupling with eq 5 made eq 4 irreversible, the relationship between E_{pc} and ν obeyed $E_{pc} = -21.03 \cdot \log(\nu) - 227.64$ ($R^2 = 0.996$) for CoPPIX@C_3N_4-strept (Figure 5A, upper inset) and $E_{pc} = -35.04 \cdot \log(\nu) - 173.47$ ($R^2 = 0.993$) for CoPPIX-strept. Thus, α could be drawn from $\Delta E_{pc} = \log(\nu) = -1.15RT/(\alpha nF) = 30/\alpha$ (293 K), whose value was 0.21 for CoPPIX@C_3N_4 and 0.71 for CoPPIX. Considering the Butler−Volmer equation: $k_f = k_f^{\Theta} \cdot \exp[(-\alpha) \cdot E_{pc} \cdot nF/RT]$ and $k_b = k_b^{\Theta} \cdot \exp[-(1-\alpha) \cdot E_{pa} \cdot nF/RT]$ and their derivation from Arrhenius law, where k_f and k_b designated as the forward and backward reaction rate, the C_3N_4-supported CoPPIX could consequently react with H_2O_2 much easier than mere CoPPIX as the ratio of Gibbs free energies $\Delta G_f/\Delta G_b > 1$. As control, "reagentless" HRP-labeled tracing tag displayed a rather poor performance on the electrocatalytic reduction of H_2O_2 with a tardy onset potential and no direct electrochemistry from its hemin cofactor (Figure 5B, curve d). According to the Koutecky−Levich equation, the apparent Michaelis−Menten constant (K_M^{app}) is determined to be 3.71 ± 0.29 mM for CoPPIX@C_3N_4 and 8.87 ± 0.38 mM for HRP. Therefore, the developed biomimetic enzyme was of high affinity and could be utilized as a competent signal tag for ECL bioassay.

3.5. Theoretical Calculations. To unveil the origin of enhanced catalytic activity and structural steadiness of CoPPIX@C_3N_4 composite catalyst, global molecular mechanical convergence (for C_3N_4) coupled with local quantum mechanical calculation (for CoPPIX) was conducted for typical five- and four-ligated models (Figure 6A,B). The axial coordination was assumed as the maximal donation of electrons from C_3N_4 to Co^{II} (Figure 6A). The binding energy of CoPPIX on C_3N_4, the adsorptive stretching of Co−N bond, and the charge density of Co^{II} on the active sites of C_3N_4 were the key parameters that could determine the rate of H_2O_2 reduction.[25]

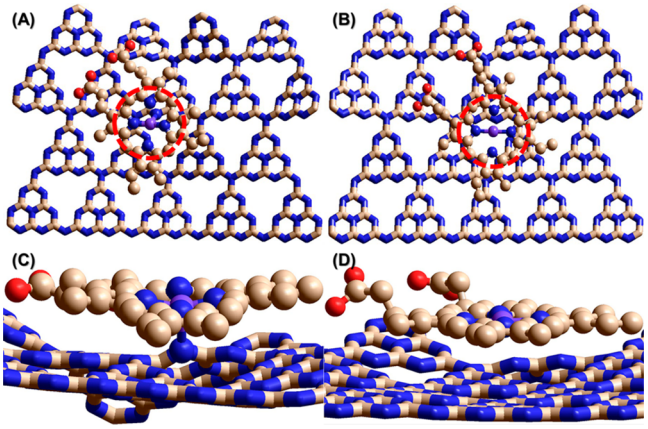

Figure 6. Overviews of optimized structure of (A) CoPPIX π-stacked on C_3N_4 and (B) CoPPIX axially ligated with C_3N_4. (C, D) Magnified side views of (A) and (B), respectively. The brown, blue, red, and violet balls and tubes represent the carbon, nitrogen, oxygen, and cobalt ion, respectively.

As a consequence of rehybridization of 3d orbitals with the bonding states, the geometrical and electronic structures of five-ligated Co−pyridinic N in C_3N_4 system (Figure 6A) were found to be very different from those four-ligated systems, e.g. the pristine CoPPIX and its π-stacking on C_3N_4 (Figure 6B). As shown in Table 3, the four-ligated cobaltic configurations with large distances between Co and graphitic/pyridinic N (l_{Co-N}) in C_3N_4 (120.6% and 90.2% longer than Co−imidazole N_4 in free CoPPIX, respectively) were observed in π-stacking systems. On the contrary, a much shorter Co−N bonding emerged in the five-ligated Co−pyridinic N system, whose length (1.94 Å) extremely approximated that in CoPPIX (1.90 Å). The equilibrium conformation also clearly illustrated that this ideal axial ligation positioned rightly upon the periodical "cavities" of C_3N_4 for minimal steric hindrance (Figure 6B). The assembling dynamics demonstrates that C_3N_4 could adjust its flexible interlinking of heptaazaphenalene units to simulate the protein folding and acted as a matrix for supporting CoPPIX from the background.

The binding energy or thermodynamically, the formation enthalpy (ΔH_f), of CoPPIX with C_3N_4 via axial coordination dropped as compared with those through $\pi-\pi$ stacking (Table 3), suggesting a favorable adsorption of CoPPIX on the active sites of pyridinic N. In addition, a higher charge density (Q) near Fermi level was obtained in this five-ligated system, which presumably facilitated the H_2O_2-reduction reaction. Notably, the embedded Co^{II} also possessed a lower spin state (S) than other listed systems, which took responsibility for the H_2O_2-reduction activity.[25] Stereochemically, the affinitive tendency between Co^{II} and pyridinic N not only assisted in stabilizing the crucial cobalt intermediate (Co^{III}−OOH) with six-paired d^2sp^3 hybridized orbitals, the enhanced electrophilicity of Co^{III} further promoted O−O polarization in heterolytic rather than homolytic splitting,[25] culminating in a synergic effect on the electroreduction of H_2O_2.

In addition, the deviation of cobalt cation from the center of porphine ring after the adsorption was critical to the stability of devised catalyst. Larger shift of Co^{II} corresponded to longer and weaker Co−N_4 bond, aggravating the probability of metallic liberation from aromatic macrocycle, which was commonly

Table 3. Calculated Energy and Structural Parameters for CoPPIX(@C_3N_4)

	l_{Co-N} (Å)	ΔH_f (kcal·mol^{-1})	Q (C)	S (Co^{II})	R_d (Å)
axial ligation: Co^{II}−pyridinic N	1.90	325.75	1.99	0.93	−0.0227
π−π stacking: Co^{II}−graphitic N	4.28	341.50	1.50	1.21	0.0032
π−π stacking: Co^{II}−pyridinic N	3.71	343.32	1.35	1.18	0.0102
coordination bond: Co^{II}−imidazole N	1.94		1.37	1.19	0

believed to be responsible for the degradation in activity.[25,47] As shown in the zoom-in molecular structure of CoPPIX@C_3N_4 (Figure 6C), the cobalt ion remained in the plane of cyclic porphyrin, almost identical to its original status (Figure 6D). The little relative displacement (R_d) of Co with electrons supplied from behind resulted in stronger Co−N_4 bonds than in the π-stacking mode (Table 3), leading to excellent stability. Moreover, compared with the four-ligated Co, the charge transfer between Co and pyridinic N in C_3N_4 also helped in diminishing the chance of cationic dissociation and in strengthening the durability.

The binding energy or thermodynamically, the formation enthalpy (ΔH_f), of CoPPIX with C_3N_4 via axial coordination dropped as compared with those through π−π stacking (Table 3), suggesting a favorable adsorption of CoPPIX on the active sites of pyridinic N. In addition, a higher charge density (Q) near Fermi level was obtained in this five-ligated system, which presumably facilitated the H_2O_2-reduction reaction. Notably, the embedded Co^{II} also possessed a lower spin state (S) than other listed systems, which took responsibility for the HRR activity.[25] Stereochemically, the affinitive tendency between Co^{II} and pyridinic N not only assisted in stabilizing the crucial cobalt intermediate (Co^{III}−OOH) with six-paired d^2sp^3 hybridized orbitals, the enhanced electrophilicity of Co^{III} further promoted O−O polarization in heterolytic rather than homolytic splitting,[25] culminating in a synergic effect on the electroreduction of H_2O_2.

In addition, the deviation of cobalt cation from the center of porphine ring (R_d) after the adsorption was critical to the stability of devised catalyst. Larger shift of Co^{II} corresponded to longer and weaker Co−N_4 bond, aggravating the probability of metallic liberation from aromatic macrocycle, which was commonly believed to be responsible for the degradation in activity.[25,47] As shown in the zoom-in molecular structure of CoPPIX@C_3N_4 (Figure 6C), the cobalt ion remained in the plane of cyclic porphyrin, almost identical to its original status (Figure 6D). The little relative displacement (R_d) of Co with electrons supplied from behind resulted in stronger Co−N_4 bonds than in the π-stacking mode (Table 3), leading to excellent stability. Moreover, compared with the four-ligated Co, the charge transfer between Co and pyridinic N in C_3N_4 also helped in diminishing the chance of cationic dissociation and in strengthening the durability.

3.6. ECL Quenching Mechanism. The GCE/QDs showed an intensive ECL emission peaking at −1.16 V in N_2-saturated pH 9.0 PBS with H_2O_2 as the exogenous coreactant (Figure 7A, curve a). Because of its good film-making capability with abundant amino groups, chitosan was employed to attach PDITC as coupling reagent for the immobilization of *c*DNA. The ECL intensities began to drop slightly during the stepwise attachment of *c*DNA and blocking agent (Figure 7A, curve b), because alkythiolated hairpins and insulating proteins impeded the mass transfer of coreactants to the underlying QDs. After the specific association of 10 pM *t*DNA with *c*DNA, the stem-loop conformation unfolded, and the steric hindrance from the

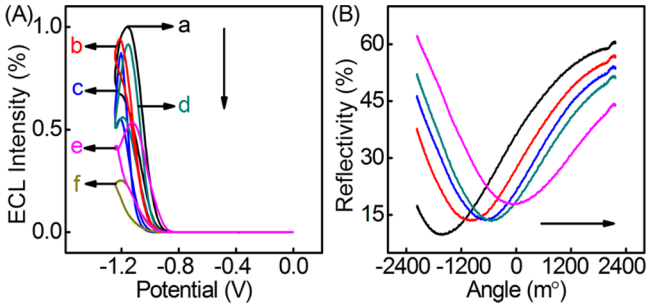

Figure 7. (A) ECL responses of GCE/QDs (a), GCE/QDs/*c*DNA/BSA (b), GCE/QDs/*c*DNA/BSA/*t*DNA (c); and (c) labeled with C_3N_4 (d), HRP (e) and CoPPIX@C_3N_4 (f) in N_2-saturated 0.1 M pH 9.0 PBS containing 50 μM H_2O_2 as the coreactant. (B) The influence of assay procedure on SPR angles. (left to right) MPA-modified monolayers on the Au surface; immobilization of *c*DNA; blocking with BSA; hybridization with *t*DNA; and labeling with CoPPIX@C_3N_4-strept.

consequent duplex further decrease the ECL signal (Figure 7A, curve c). As strong adsorption of H_2O_2 onto C_3N_4 was reported,[48] the ECL intensity restored somewhat in the presence of C_3N_4-strept (Figure 7A, curve d). Although C_3N_4 was capable of ECL irradiation, it emitted anodically only if considerable amount (mg) was used as substrate.[49] As expected, the ECL intensity declined by 45.5% with HRP labeling (Figure 7A, curve e). On the contrary, the ECL response was annihilated to its original 23.6% after incubation with the fabricated probe despite the existence of C_3N_4 (Figure 7A, curve f), indicating a totally different quenching mechanism other than the steric hindrance. Obviously, it correlated to the preconsumption of H_2O_2 in a catalytic reduction pathway, preventing its participation in ECL reactions, as the proposed CoPPIX@C_3N_4-strept has been proved of biomimetic activity. Its quenching effect on ECL was quite superior to that of HRP-strept, which was consistent with their electrocatalytic discrepancy visualized in Figure 5B. The developed strategy could thus realize a ultrasensitive detection of DNA.

3.7. Characterization of DNA Sensor. The stepwise fabrication and the recognition of the proposed DNA assay were further confirmed by SPR technique, since surface plasmons are sensitive to the changes of interfacial mass and local refractivity within approximately 300 nm of the surface.[50] To simulate the sensing protocol, the gold disk was first modified ex situ with a self-assembled monolayer of mercaptopropionic acid and further exposed in situ to subsequent injections of *c*DNA, BSA, *t*DNA, and the signal probe with a pumping rate of 10 μL s^{-1} at 37 °C. Each step was real-time monitored until the access to saturated bindings followed by rinsing. The extents of assembly and hybridization were expressed as the shifts of SPR angles (θ_r) as shown in Figure 7B. The self-assembled substrate of thiols as the blank showed a θ_r of −1633.708 m°. The angle began moving positively as the stepwise immobilization of 1.0 μM *c*DNA at (−995.450 m°), the blocking of unspecific sites with BSA

(−669.331 m°), the direct hybridization with 0.1 nM *t*DNA (−538.662 m°), and finally the labeling with CoPPIX@C_3N_4-strept (−54.432 m°). As no electronic coupling happens between the localized probe and the Au film-associated surface plasmon wave,[51] the unidirectional shift indicated the gradual accumulation of mass near the sensor surface, thus confirming the successful fabrication of DNA sensor. The most remarkable change in SPR angles appeared between the last two steps, which suggested otherwise that the ECL quenching did not result from the probe-induced steric hindrance.

3.8. Optimization of Detection Conditions. To apply the proposed method in ECL DNA assay, several experimental parameters should be optimized including the solution pH and the incubation time of *t*DNA. The effect of detection solution pH on the ECL response of QDs is shown in Figure 8A. In the examined pH range, the ECL intensity increased with the increasing pH value and then reached a maximum at pH 9.0. A PBS of such pH was selected as the detection solution.

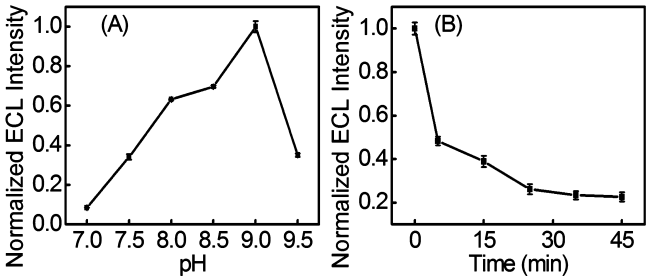

Figure 8. Effects of (A) pH value of detection solution and (B) incubation time for *t*DNA on ECL intensity of CoPPIX@C_3N_4 bound DNA sensor in N_2-saturated 0.1 M pH 9.0 PBS containing 50 μM H_2O_2.

With the increasing incubation time at 37 °C for the hybridization of *c*DNA to *t*DNA, the ECL intensity diminished drastically, which was due to the subsequent tagging blocking coreactants contacting QDs, and treaded a plateau at ∼30 min (Figure 8B), demonstrating a saturated binding between the analyte and *c*DNA on the sensing surface. Therefore, 30 min of incubation time was implemented for the DNA assay. In addition, to guarantee the maximal formation of double-stranded DNA, the concentration of *c*DNA for a saturated immobilization on the chitosan membrane was settled at 1.0 μM.

3.9. ECL-based DNA Sensing and Analytical Performance. Taking advantage of the efficient ECL emission of DMPS-CdTe QDs, a facile "signal-off" strategy was proposed for the detection of *t*DNA based on the consumption of coreactant. As shown in Figure 9A, the ECL peak intensity decreased with the increasing *t*DNA concentration. Under the optimum conditions, the calibration plot showed a good linear relationship between the ECL intensity and the logarithm value of the target concentration ranging from 0.1 fM to 0.1 nM with a correlation coefficient of 0.994 (Figure 9A inset). The detection limit at a signal-to-noise ratio of 3 was 8.2×10^{-2} fM, which was at least 20 times lower than those previously reported by silver nanocluster-enhanced surface-enhanced Raman, hemin-*G*-quadruplex catalyzed chemiluminescence, and ECL techniques with palladium nanoparticles as enzymeless labels.[52−55] More importantly, the developed DNA sensor showed a wide detection range of 6 orders of magnitude and could be expanded in general electrochemical bioassays.

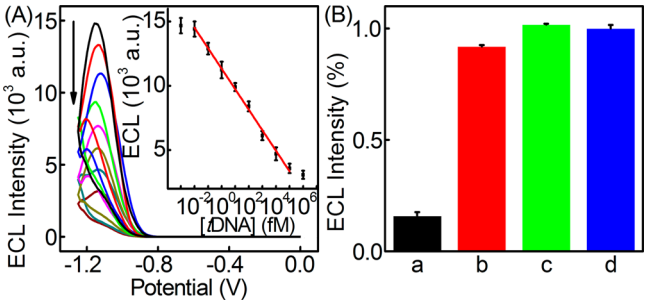

Figure 9. (A) ECL responses of the proposed DNA sensor to *t*DNA at 0, 0.1 fM, 1.0 fM, 10.0 fM, 0.1 pM, 1.0 pM, 10.0 pM, and 0.1 nM (from top to bottom) in N_2-saturated 0.1 M pH 9.0 PBS containing 50 μM H_2O_2 as the coreactant. (inset) Calibration curve (n = 3). (B) ECL quenching of GCE/QDs/*c*DNA/BSA after the successive incubation with 20 μL of 0.1 nM DNA/*t*DNA (a), partial complementary 1-mismatch (b), 2-mismatch (c), and 3-mismatch (d); and then the tracing tag.

Both the intra-assay and interassay precisions of the ECL DNA sensor were examined by detecting 10 pM *t*DNA. The relative standard deviation (RSD) for 20 measurements of *t*DNA with the same sensor was 7.1%, while the RSD for 20 parallel measurements with 20 sensors was 9.6%, indicating good precision of the assay method and acceptable fabrication reproducibility of the DNA sensors. Fifty measurements of ECL emission upon continuous cyclic scans of the ECL immunosensor for 10 pM *t*DNA showed coincident signal with RSD of 0.88%, indicating good reliability and stability of the detection signal.

The DNA sensor showed good specificity for sequence detection of the *t*DNA. After the mixture of 10 pM one-, two-, or three-base mismatched DNA oligonucleotide was dropped on GCE/QDs/*c*DNA/BSA for hybridization, the proposed biosensor showed much weaker ECL variations than that hybridized with complementary DNA at the same concentration. The corresponding quenching percentages resulting from the three sequences were 8.1%, −2.7%, and 1.7% with respect to that for the complementary *t*DNA, respectively (Figure 9B).

4. CONCLUSIONS

This work demonstrated a convenient way to rationally synthesize and functionalize the CoPPIX@C_3N_4 complex. It possesses much higher peroxidase-like catalytic activity and faster catalytic kinetics than most porphyrin-based mimetic enzymes. The π-donor from monolayered C_3N_4 nanocarrier can preserve the primordial enzymatic environment and at the same time improve the stability against the degradation of cofactors in catalysis. Its highly efficient electrocatalytic activity toward the reduction of H_2O_2 prevailed over that of HRP, which greatly prohibits the coreactant route of H_2O_2 and quenches the QDs-based ECL emission. By coupling with this consumption mechanism, the biomimetic enzyme can be linked with molecular beacon to achieve signal amplification and perform an ultrasensitive ECL detection of DNA, resulting in a wide linear range over 6 orders of magnitude and a detection limit of sub-femtomolar. Because of the outstanding advantages of CoPPIX@C_3N_4, this novel enzyme mimic can be easily

hyphenated with other amplification strategies for applications in different fields.

AUTHOR INFORMATION

Corresponding Author

*Phone/Fax: +86-25-84303107. E-mail: danshan@njust.edu.cn.

Author Contributions

[§]These authors contributed equally.

Notes

The authors declare no competing financial interest.

ACKNOWLEDGMENTS

This research was supported by National Natural Science Foundation of China (Grant No. 21175114, 21305067), Natural Science Foundation of Jiangsu Province (BK2011441, 20130754), Ph.D. Fund of MOE for Young Teachers (0133219120019), the Fundamental Research Funds for the Central Universities (30920140112009), and State Key Laboratory of Analytical Chemistry for Life science (SKLACLS1302).

REFERENCES

(1) Cibulskis, K.; Lawrence, M. S.; Carter, S. L.; Sivachenko, A.; Jaffe, D.; Sougnez, C.; Gabriel, S.; Meyerson, M.; Lander, E. S.; Getz, G. Sensitive Detection of Somatic Point Mutations in Impure and Heterogeneous Cancer Samples. *Nat. Biotechnol.* **2013**, *31*, 213−219.

(2) Pattanayak, V.; Lin, S.; Guilinger, J. P.; Ma, E. B.; Doudna, J. A.; Liu, D. R. High-Throughput Profiling of Off-Target DNA Cleavage Reveals RNA-Programmed Cas9 Nuclease Specificity. *Nat. Biotechnol.* **2013**, *31*, 839−843.

(3) DeKosky, B. J.; Ippolito, G. C.; Deschner, R. P.; Lavinder, J. J.; Wine, Y.; Rawlings, B. M.; Varadarajan, N.; Giesecke, C.; Dorner, T.; Andrews, S. F. High-Throughput Sequencing of the Paired Human Immunoglobulin Heavy and Light Chain Repertoire. *Nat. Biotechnol.* **2013**, *31*, 166−169.

(4) Ma, D.L.; He, H. Z.; Leung, K. H.; Zhong, H. J.; Chan, D. S.-H.; Leung, C. H. Label-Free Luminescent Oligonucleotide-Based Probes. *Chem. Soc. Rev.* **2013**, *42*, 3427−3440.

(5) Feng, L. Y.; Wu, L.; Qu, X. G. New Horizons for Diagnostics and Therapeutic Applications of Graphene and Graphene Oxide. *Adv. Mater.* **2013**, *25*, 168−186.

(6) Du, Y.; Li, B. L.; Wang, E. K. "Fitting" Makes "Sensing" Simple: Label-Free Detection Strategies Based on Nucleic Acid Aptamers. *Acc. Chem. Res.* **2013**, *46*, 203−213.

(7) Zhou, X. M.; Zhu, D. B.; Liao, Y. H.; Liu, W. P.; Liu, H. X.; Ma, Z. K.; Xing, D. Synthesis, Labeling and Bioanalytical Applications of a Tris(2,2′-bipyridyl) ruthenium(II)-Based Electrochemiluminescence Probe. *Nat. Protoc.* **2014**, *9*, 1146−1159.

(8) Deng, S. Y.; Ju, H. X. Electrogenerated Chemiluminescence of Nanomaterials for Bioanalysis. *Analyst* **2013**, *138*, 43−61.

(9) Wang, J.; Han, H. Y. Near-Infrared Electrogenerated Chemiluminescence from Quantum Dots. *Rev. Anal. Chem.* **2013**, *32*, 91−101.

(10) Xu, J. J.; Zhao, W. W.; Song, S. P.; Fan, C. H.; Chen, H. Y. Functional Nanoprobes for Ultrasensitive Detection of Biomolecules: An Update. *Chem. Soc. Rev.* **2014**, *43*, 1601−1611.

(11) Rusling, J. F. Multiplexed Electrochemical Protein Detection and Translation to Personalized Cancer Diagnostics. *Anal. Chem.* **2013**, *85*, 5304−5310.

(12) Mani, V.; Wasalathanthri, D. P.; Joshi, A. A.; Kumar, C. V.; Rusling, J. F. Highly Efficient Binding of Paramagnetic Beads Bioconjugated with 100000 or More Antibodies to Protein-Coated Surfaces. *Anal. Chem.* **2012**, *84*, 10485−10491.

(13) Krishnan, S.; Mani, V.; Wasalathanthri, D.; Kumar, C. V.; Rusling, J. F. Attomolar Detection of a Cancer Biomarker Protein in Serum by Surface Plasmon Resonance Using Superparamagnetic Particle Labels. *Angew. Chem., Int. Ed.* **2011**, *50*, 1175−1178.

(14) Ogi, S.; Sugiyasu, K.; Manna, S.; Samitsu, S.; Takeuchi, M. Living Supramolecular Polymerization Realized Through a Biomimetic Approach. *Nat. Chem.* **2014**, *6*, 188−195.

(15) Arai, T.; Tanaka, M.; Kawakami, H. Porphyrin-Containing Electrospun Nanofibers: Positional Control of Porphyrin Molecules in Nanofibers and Their Catalytic Application. *ACS Appl. Mater. Interfaces* **2012**, *4*, 5453−5457.

(16) Kanaizuka, K.; Izumi, A.; Ishizaki, M.; Kon, H.; Togashi, T.; Miyake, R.; Ishida, T.; Tamura, R.; Haga, M.; Moritani, Y.; Sakamoto, M.; Kurihara, M. Molecular Nanostamp Based on One-Dimensional Porphyrin Polymers. *ACS Appl. Mater. Interfaces* **2013**, *5*, 6879−6885.

(17) Wang, F.; Lu, C. H.; Willner, I. From Cascaded Catalytic Nucleic Acids to Enzyme−DNA Nanostructures: Controlling Reactivity, Sensing, Logic Operations, and Assembly of Complex Structures. *Chem. Rev.* **2014**, *114*, 2881−2941.

(18) Lu, C. H.; Willner, B.; Willner, I. Biocatalytic Release of an Anticancer Drug from Nucleic-Acids-Capped Mesoporous SiO_2 Using DNA or Molecular Biomarkers as Triggering Stimuli. *ACS Nano* **2014**, *7*, 8320−8332.

(19) Sun, Y. H.; Benabbas, A.; Zeng, W. Q.; Kleingardner, J. G.; Bren, K. L.; Champion, P. M. Heme-Protein Vibrational Couplings in Cytochrome *c* Provide a Dynamic Link that Connects the Heme-Iron and the Protein Surface. *Proc. Natl. Acad. Sci. U.S.A.* **2014**, *111*, 6570−6575.

(20) Anderson, J. L. R.; Armstrong, C. T.; Kodali, G.; Lichtenstein, B. R.; Watkins, D. W.; Mancini, J. A.; Boyle, A. L.; Farid, T. A.; Crump, M. P.; Moser, C. C. Constructing a Man-Made *c*-Type Cytochrome Maquette *in vivo*: Electron Transfer, Oxygen Transport and Conversion to a Photoactive Light Harvesting Maquette. *Chem. Sci.* **2014**, *5*, 507−514.

(21) den Boer, D.; Li, M.; Habets, T.; Iavicoli, P.; Rowan, A. E.; Nolte, R. J. M.; Speller, S.; Amabilino, D. B.; De Feyter, S.; Elemans, J. A. A. W. Detection of Different Oxidation States of Individual Manganese Porphyrins during Their Reaction with Oxygen at a Solid/Liquid Interface. *Nat. Chem.* **2013**, *5*, 621−627.

(22) Wang, X. S.; Peter, S.; Ullrich, R.; Hofrichter, M.; Groves, J. T. Driving Force for Oxygen-Atom Transfer by Heme-Thiolate Enzymes. *Angew. Chem., Int. Ed.* **2013**, *52*, 9238−9241.

(23) Wei, H.; Wang, E. K. Nanomaterials with Enzyme-Like Characteristics (Nanozymes): Next-Generation Artificial Enzymes. *Chem. Soc. Rev.* **2013**, *42*, 6060−6093.

(24) Deng, S. Y.; Lei, J. P.; Huang, Y.; Cheng, Y.; Ju, H. X. Electrochemiluminescent Quenching of Quantum Dots for Ultrasensitive Immunoassay through Oxygen Reduction Catalyzed by Nitrogen-Doped Graphene-Supported Hemin. *Anal. Chem.* **2013**, *85*, 5390−5396.

(25) Cao, R. G.; Thapa, R.; Kim, H.; Xu, X. D.; Kim, M. G.; Li, Q.; Park, N.; Liu, M. L.; Cho, J. Promotion of Oxygen Reduction by a Bio-Inspired Tethered Iron Phthalocyanine Carbon Nanotube-Based Catalyst. *Nat. Commun.* **2013**, *4*, 2076−2782.

(26) Xue, T.; Jiang, S.; Qu, Y. Q.; Su, Q.; Cheng, R.; Dubin, S.; Chiu, C. Y.; Kaner, R.; Huang, Y.; Duan, X. F. Graphene-Supported Hemin as a Highly Active Biomimetic Oxidation Catalyst. *Angew. Chem., Int. Ed.* **2012**, *124*, 3888−3891.

(27) Ragoussi, M. E.; Katsukis, G.; Roth, A.; Malig, J.; de la Torre, G.; Guldi, D. M.; Torres, T. Electron-Donating Behavior of Few-Layer Graphene in Covalent Ensembles with Electron-Accepting Phthalocyanines. *J. Am. Chem. Soc.* **2014**, *136*, 4593−4598.

(28) Xu, M. S.; Liang, T.; Shi, M. M.; Chen, H. Z. Graphene-Like Two-Dimensional Materials. *Chem. Rev.* **2013**, *113*, 3766−3798.

(29) Tian, J. Q.; Liu, Q.; Asiri, A. M.; Al-Youbi, A. O.; Sun, X. P. Ultrathin Graphitic Carbon Nitride Nanosheet: A Highly Efficient Fluorosensor for Rapid, Ultrasensitive Detection of Cu^{2+}. *Anal. Chem.* **2013**, *85*, 5595−5599.

(30) Toraya, T. G-Protein Signaling: A Switch Saves B12 Radical Status. *Nat. Chem. Biol.* **2013**, *9*, 530−531.

(31) Lofgren, M.; Padovani, D.; Koutmos, M.; Banerjee, R. The DNA-Binding Domain Mediates Both Nuclear and Cytosolic Functions of p53. *Nat. Chem. Biol.* **2013**, *9*, 535−543.
(32) Xu, J.; Wu, J.; Zong, C.; Ju, H. X.; Yan, F. Manganese Porphyrin-*ds*DNA Complex: A Mimicking Enzyme for Highly Efficient Bioanalysis. *Anal. Chem.* **2013**, *85*, 3374−3379.
(33) Wu, H.; Fan, S. H.; Jin, X. Y.; Zhang, H.; Chen, H.; Dai, Z.; Zou, X. Y. Construction of a Zinc Porphyrin−Fullerene-Derivative Based Nonenzymatic Electrochemical Sensor for Sensitive Sensing of Hydrogen Peroxide and Nitrite. *Anal. Chem.* **2014**, *86*, 6285−6290.
(34) Yang, S. B.; Gong, Y. J.; Zhang, J. S.; Zhan, L.; Ma, L. L.; Fang, Z. Y.; Vajtai, R.; Wang, X. C.; Ajayan, P. M. Exfoliated Graphitic Carbon Nitride Nanosheets as Efficient Catalysts for Hydrogen Evolution under Visible Light. *Adv. Mater.* **2013**, *25*, 2452−2456.
(35) Niu, P.; Zhang, L. L.; Liu, G.; Cheng, H.-M. Graphene-Like Carbon Nitride Nanosheets for Improved Photocatalytic Activities. *Adv. Funct. Mater.* **2012**, *22*, 4763−4770.
(36) Deng, S. Y.; Zhang, T. T.; Zhang, Y.; Shan, D.; Zhang, X. J. Chronopotentiometric Synthesis of Quantum Dots with Efficient Surface-Derived Near-Infrared Electro- chemiluminescence for Ultra-sensitive Microchip-Based Ion-Selective Sensing. *RSC Adv.* **2014**, *4*, 29239−29248.
(37) Simons, W. W. *The Sadtler Handbook of Infrared Spectra,* 1st ed; Sadtler Research Laboratories: Philadelphia, PA, 1978.
(38) Mou1der, J. F.; Stickle, W. F.; Sobol, P. E.; Bomben, K. D. *Handbook of X-ray Photoelectron Spectroscopy: A Reference Book of Standard Spectra for Identification and Interpretation of XPS Data,* 1st ed; Perkin-Elmer Corporation: Minnesota, MN, 1992.
(39) Yosca, T. H.; Behan, R. K.; Krest, C. M.; Onderko, E. L.; Langston, M. C.; Green, M. T. Setting an Upper Limit on the Myoglobin Iron(IV)Hydroxide pK_a: Insight into Axial Ligand Tuning in Heme Protein Catalysis. *J. Am. Chem. Soc.* **2014**, *136*, 9124−9131.
(40) Hassanpour, A.; Miguel, D. R.-S.; Fierro, J. L. G.; Horrocks, B. R.; Mas-Ballesté, R.; Zamora, F. Supramolecular Attachment of Metalloporphyrins to Graphene Oxide and Its Pyridine-Containing Derivative. *Chem.—Eur. J.* **2013**, *19*, 10463−10467.
(41) Lefèvre, M.; Dodelet, J. P.; Bertrand, P. Molecular Oxygen Reduction in PEM Fuel Cells: Evidence for the Simultaneous Presence of Two Active Sites in Fe-Based Catalysts. *J. Phys. Chem. B* **2002**, *106*, 8705−8713.
(42) Xu, Y. X.; Zhao, L.; Bai, H.; Hong, W. J.; Li, C.; Shi, G. Q. Chemically Converted Graphene Induced Molecular Flattening of 5,10,15,20-Tetrakis(1-methyl-4-pyridinio) porphyrin and Its Application for Optical Detection of Cadmium(II) Ions. *J. Am. Chem. Soc.* **2009**, *131*, 13490−13497.
(43) Yamaguchi, H.; Tsubouchi, K.; Kawaguchi, K.; Horita, E.; Harada, A. Peroxidase Activity of Cationic Metalloporphyrin-Antibody Complexes. *Chem.—Eur. J.* **2004**, *10*, 6179−6186.
(44) Wang, Q. G.; Yang, Z. M.; Zhang, X. Q.; Xiao, X. D.; Chang, C. K.; Xu, B. A Supramolecular-Hydrogel-Encapsulated Hemin as an Artificial Enzyme to Mimic Peroxidase. *Angew. Chem., Int. Ed.* **2007**, *46*, 4285−4289.
(45) Wang, Q. G.; Yang, Z. M.; Ma, M.; Chang, C. K.; Xu, B. High Catalytic Activities of Artificial Peroxidases Based on Supramolecular Hydrogels That Contain Heme Models. *Chem.—Eur. J.* **2008**, *14*, 5073−5078.
(46) Wang, Q. B.; Lei, J. P.; Deng, S. Y.; Zhang, L.; Ju, H. X. Graphene-Supported Ferric Porphyrin as a Peroxidase Mimic for Electrochemical DNA Biosensing. *Chem. Commun.* **2013**, *49*, 916−918.
(47) Tang, H. J.; Yin, H. J.; Wang, J. Y.; Yang, N. L.; Wang, D.; Tang, Z. Y. Molecular Architecture of Cobalt Porphyrin Multilayers on Reduced Graphene Oxide Sheets for High-Performance Oxygen Reduction Reaction. *Angew. Chem., Int. Ed.* **2013**, *52*, 5585−5589.
(48) Chen, L. C.; Zeng, X. T.; Si, P.; Chen, Y. M.; Chi, Y. W.; Kim, D. H.; Chen, G. N. Gold Nanoparticle-Graphite-Like C_3N_4 Nanosheet Nanohybrids Used for Electrochemiluminescent Immunosensor. *Anal. Chem.* **2014**, *86*, 4188−4195.
(49) Cheng, C. M.; Huang, Y.; Wang, J.; Zheng, B. Z.; Yuan, H. Y.; Xiao, D. Anodic Electrogenerated Chemiluminescence Behavior of Graphite-Like Carbon Nitride and Its Sensing for Rutin. *Anal. Chem.* **2013**, *85*, 2601−2605.
(50) Abadian, P. N.; Kelley, C. P.; Goluch, E. D. Cellular Analysis and Detection Using Surface Plasmon Resonance Techniques. *Anal. Chem.* **2014**, *86*, 2799−2812.
(51) Kwon, M. J.; Lee, J.; Wark, A. W.; Lee, H. J. Nanoparticle-Enhanced Surface Plasmon Resonance Detection of Proteins at Attomolar Concentrations: Comparing Different Nanoparticle Shapes and Sizes. *Anal. Chem.* **2012**, *84*, 1702−1707.
(52) Gao, F. L.; Lei, J. P.; Ju, H. X. Label-Free Raman Spectroscopy for Sensitive DNA Detection by DNA-Mediated Silve Nanoparticle Growth. *Anal. Chem.* **2013**, *85*, 11788−11793.
(53) Dong, H. F.; Jin, S.; Ju, H. X.; Hao, K. H.; Xu, L. P.; Lu, H. T.; Zhang, X. J. Trace and Label-Free MicroRNA Detection Using Oligonucleotide Encapsulated Silver Nanoclusters as Probes. *Anal. Chem.* **2012**, *84*, 8670−8674.
(54) Zong, C.; Wu, J.; Liu, M. M.; Yang, L. L.; Liu, L.; Yan, F.; Ju, H. X. Proximity Hybridization-Triggered Signal Switch for Homogeneous Chemiluminescent Bioanalysis. *Anal. Chem.* **2014**, *86*, 5573−5578.
(55) Deng, S. Y.; Lei, J. P.; Huang, Y.; Yao, X. N.; Ding, L.; Ju, H. X. Electrocatalytic Reduction of Coreactant by Highly Loaded Dendrimer-Encapsulated Palladium Nanoparticles for Sensitive Electrochemiluminescent Immunoassay. *Chem. Commun.* **2012**, *48*, 9159−9161.